

Self-Powered Sensing for Smart Agriculture by Electromagnetic–Triboelectric Hybrid Generator

Baosen Zhang,[¶] Sheng Zhang,[¶] Wenbo Li, Qi Gao, Da Zhao, Zhong Lin Wang,^{*} and Tinghai Cheng^{*}



Cite This: <https://doi.org/10.1021/acsnano.1c08417>



Read Online

ACCESS |



Metrics & More



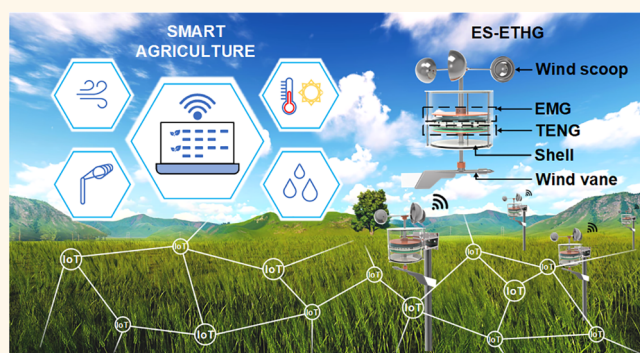
Article Recommendations



Supporting Information

ABSTRACT: The lack of efficient, low-cost, distributed energy collection methods is a vital factor restricting the application of the Internet of Things (IoT) in smart agriculture. This paper proposes a method based on triboelectric nanogenerator and electromagnetic generator to realize self-powered IoT nodes and self-powered sensors at the same time. An energy harvesting and sensing device based on electromagnetic-triboelectric hybrid generator (ES-ETHG) is designed. The peak power of ES-ETHG is 32.4 mW, which can supply power to IoT nodes for a long time with power management circuits. In addition, ES-ETHG can critically measure wind speed and wind level within the range of 3–15 m/s, and accurately detect wind direction within 2 s. Furthermore, the self-powered distributed weather sensing system based on ES-ETHG is developed to realize the remote collection of wind speed, wind direction, temperature, and humidity. This work proposes a solution for developing self-powered IoT and sensor in the field of smart agriculture.

KEYWORDS: Internet of Things, triboelectric nanogenerator, electromagnetic generator, smart agriculture, self-powered



Smart agriculture plays an irreplaceable role in modern society. Long-term, real-time, and accurate agricultural information sensing technology is a prerequisite for the realization of smart agriculture.^{1–3} Traditional agricultural sensing relies on weather stations, manual sensing, and fixed monitoring points. Because of human resource constraints and few sampling points, accurate sensing cannot be achieved.⁴ Recent improvements in the Internet of Things (IoT) provide opportunities for smart agriculture.^{5,6} Massive IoT nodes can provide sensor networks for agricultural production. Traditional IoT nodes rely on cables, batteries, or solar energy.⁷ However, cable installation and maintenance are inconvenient, replacing batteries wastes human resources, discarded batteries cause environmental pollution, and solar energy cannot work around the clock. At the same time, agricultural production is sensitive to the price of IoT nodes. Therefore, a cheaper self-powered solution for IoT nodes is a major challenge for smart agricultural sensor networks nowadays.

For IoT nodes, realizing self-powered nodes requires that the average power collection is greater than the average power consumption. Collecting energy from the surrounding environment, such as wind energy,^{8–11} water energy,^{12–14} and storing energy in energy storage, to supply IoT nodes is the

furthermost likely way to achieve self-powered IoT nodes.^{15,16} Besides, the power is mainly consumed by various sensors and signal processing devices. The replacement of active sensors by self-powered sensors can reduce the power consumption of IoT nodes.¹⁷ In 2012, a triboelectric nanogenerator (TENG) with high voltage, high energy conversion efficiency, and low cost was proposed by Wang's group, which attracted widespread attention in the fields of energy harvesting and self-powered sensing.^{18–22} On the basis of the coupling of triboelectrification effect and electrostatic induction, TENG can convert various weak mechanical energy into electrical energy so they can be used as highly sensitive self-powered sensors to monitor various mechanical movements^{23–32} including rotation,²⁸ touching,²⁹ sliding,³⁰ vibrations,³¹ and so on. The electromagnetic generator (EMG)

Received: September 24, 2021

Accepted: November 23, 2021

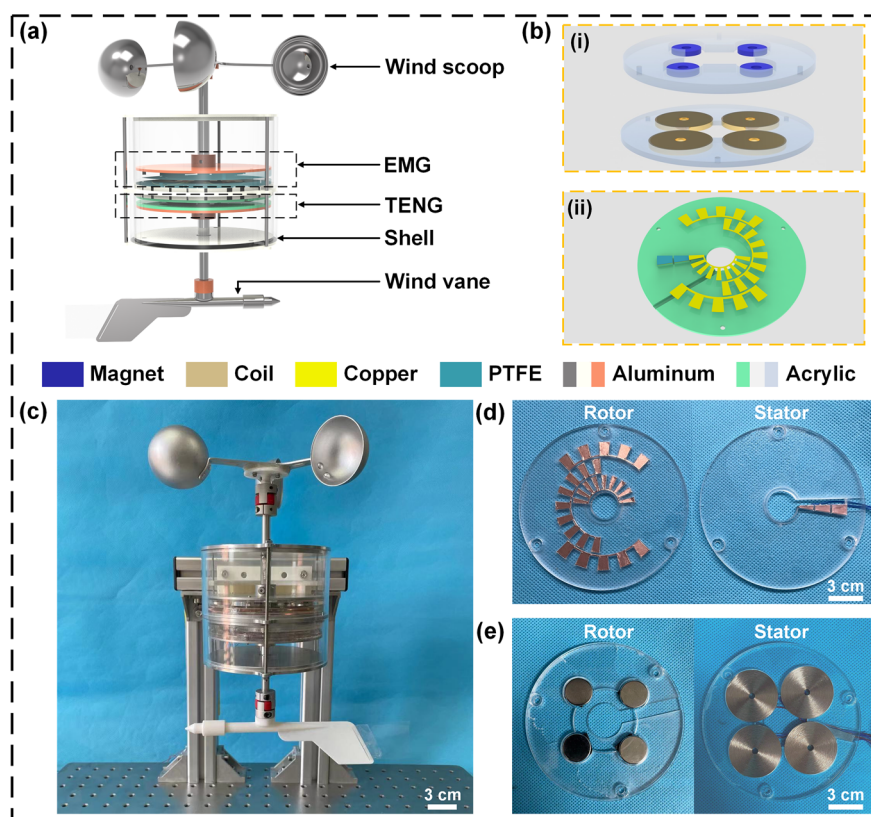


Figure 1. Structural design of sensing unit for ES-ETHG. (a) Schematic configuration of ES-ETHG. (b) Schematic diagram of (i) EMG and (ii) TENG. (c) Photograph of ES-ETHG device. (d) Rotor and stator of TENG. (e) Rotor and stator of EMG.

based on the principle of electromagnetic induction is a device that converts the work done by power into electrical energy.^{33,34} It holds the characteristics of a large current and stable output. In previous studies, TENG and EMG have been proposed for self-powered IoT nodes.^{35–37} However, they are not suitable for simultaneous energy harvesting due to the considerable power difference between the two. For self-powered IoT nodes, it is important to increase the collected energy and minimize the power of the sensor as possible. Therefore, a comprehensive strategy is urgently required to suitably combine TENG and EMG to extend the working time of IoT nodes.

Here, a method of using TENG and EMG as both energy harvesting devices and self-powered sensors to realize the self-powered IoT nodes and sensors is proposed. On the basis of this approach, an energy harvesting and sensing device based on an electromagnetic–triboelectric hybrid generator (ES-ETHG) is designed to collect wind energy and act as a wind speed and wind direction self-powered sensor. The peak power of ES-ETHG is 32.4 mW, which can provide a stable power supply for a microcontroller unit (MCU) and a temperature and humidity sensor (THS) combined with energy management circuits. ES-ETHG can measure wind speed in the range of 3–15 m/s through signal frequency. The wind direction information is obtained by analyzing the signal of TENG within 2 s. A self-powered distributed weather sensing system (SDWS) was further developed for smart agriculture to realize meteorological information collection and wireless transmission. SDWS can be flexibly installed in complex terrain without additional cables or batteries. Therefore, this method has reference value for the design and development of IoT nodes. ES-ETHG provides a possibility for IoT nodes and self-

powered sensing, making IoT and agriculture more intelligent and efficient.

RESULTS AND DISCUSSION

Structural Design and Operation Principle. Figure 1a shows that ES-ETHG is assembled from two parts, EMG and TENG. The EMG part consists of a stator and a rotor (Figure 1b(i)). The stator is composed of four coils with a diameter of 35 mm. The difference between two adjacent coils is 90°. The coils are fixed on an acrylic plate with grooves. The acrylic plate is fixed on the shell by screws to facilitate replacement and decrease maintenance. The rotor is composed of an acrylic plate with four magnets of the same polarity. It is fixed on the shaft by screws and keys. The shaft of the EMG part is connected to the wind scoop so that it can rotate with the wind scoop. The TENG part is composed of a stator and a rotor [Figure 1b(ii)]. The stator is the content of three laminations: a cut acrylic disc serves as the bottom support layer, three copper foil sectors as the energization layer, and finally, a 0.13 mm thick polytetrafluoroethylene (PTFE) film covered the copper foil. The rotor is an acrylic disc, covered with a collection of separated copper foil sectors arranged radially. The schematic flowchart of manufacturing ES-ETHG is shown in Figure S1. To better describe the inner construction of the sensor, the overall structure of the ES-ETHG unit is shown in Figure 1c, while the stator and rotor structures of the TENG part and EMG part are shown in Figure 1d and e.

The EMG part is based on the principle of electromagnetic induction, which generates periodic alternating current (AC) due to the periodic change of magnetic flux. In Figure 2a, the coil is located between the two magnets, and there is no

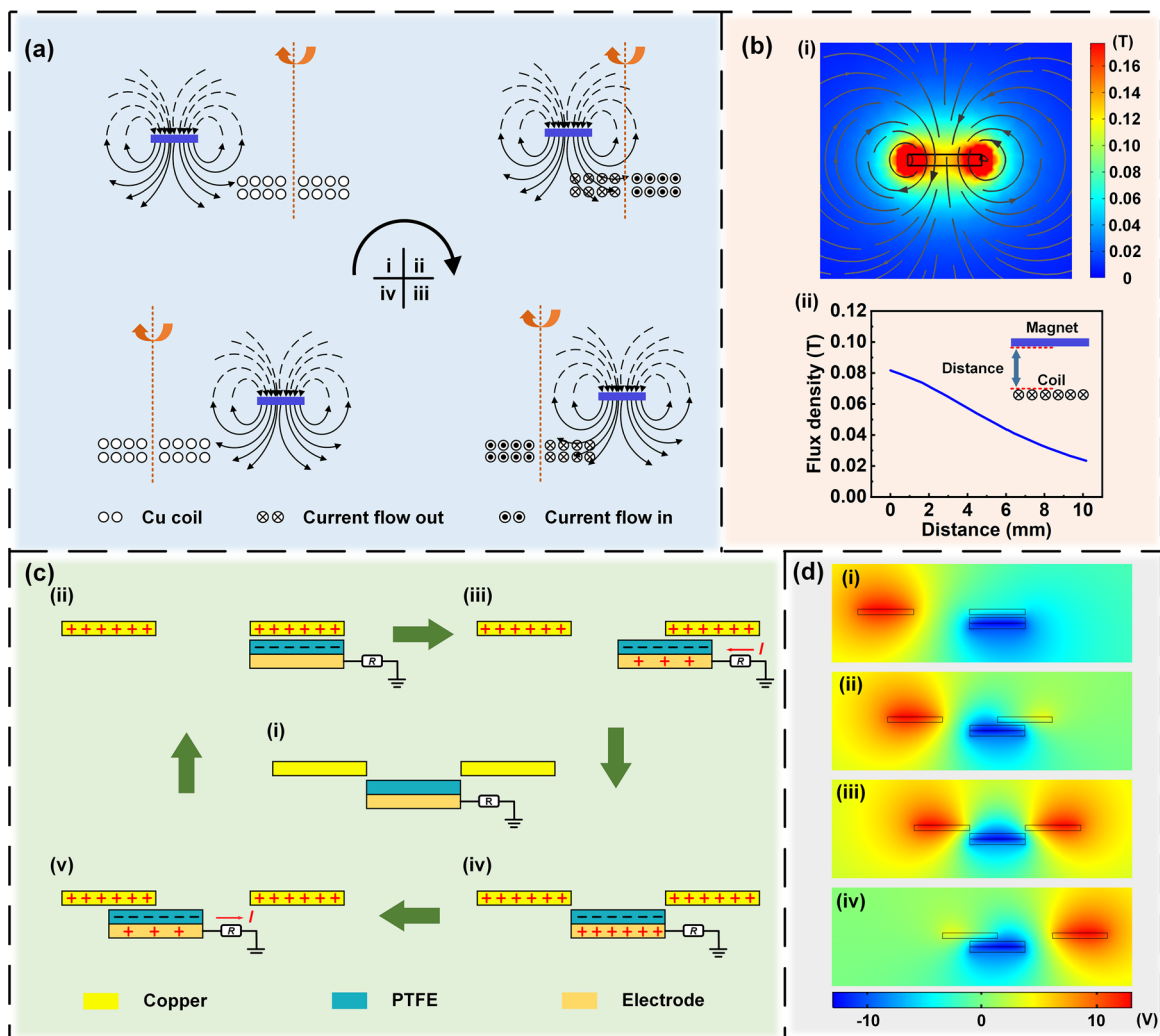


Figure 2. Working mechanism and potential distribution simulation of ES-ETHG. (a) Simulated distribution of magnetic induction lines of EMG and the direction of coil induced current at four typical situations. (b) Magnetic flux distribution of the cylindrical magnet in the EMG is simulated by COMSOL. (c) Operating principle and (d) potential distribution of TENG in four different states is simulated.

change in magnetic flux, so the induced current is zero (step (i)). When the magnet rotates around the axis, as the separation distance between the coil and the magnet decreases, the magnetic flux in the coil increases, generating an induced current in the circular copper coil. During the approach, the current continues to flow until the magnet and coil are perfectly aligned (step (ii)). As the movement continues, the separation distance between the coil and the magnet increases, and the magnetic flux in the coil decreases, thereby generating a back-induced current (step (iii)). Then the rotor continues to rotate to reach a position where the magnetic flux does not change, and there is no induced current in the coil (step (iv)). With continuous rotational movement, EMG generates continuous alternating current. In addition, the finite element study of the magnetic field of cylindrical magnets is carried out using COMSOL (COMSOL Multiphysics 5.6). The magnetic flux density distribution in the vertical direction at the center of magnet is obtained. Figure 2b(i) shows the simulated distribution of magnetic flux density of a cylindrical magnet. To optimize the electrical output of EMG, the magnetic flux density relative to the longitudinal distance of magnet is graphed [Figure 2b(ii)]. The simulation outcomes show that the magnetic flux density decreases as the distance from the

magnet increases, which significantly affects the output of EMG. Similarly, the experimental findings also show the same trend (Figure S2). Therefore, the coil should be fixed as close as possible to the magnet to improve the output performance of EMG. In Figure 2c, the copper forms three concentric grid-like copper rings on the acrylic disk, and the three rings form a TENG with three sensing channels (step (i)). Because of the huge discrepancy in triboelectricity, PTFE obtains electrons from grid-like copper and exhibits negative electricity, and grid-like copper and PTFE have the same number of different charges on their surfaces. The negative electrons are evenly distributed on the PTFE membrane and can be kept for a long time. Because of electrostatic induction, the negative charge on the copper electrode reaches the maximum when the copper sector is aligned with PTFE (step (ii)). As the rotor rotates, the copper sector gradually moves away from the PTFE, and more positive charges will accumulate on the electrode surface to shield the negative charges on the PTFE (step (iii)). When the PTFE faces the blank on the rotor, the negative charge on the PTFE will be completely shielded from the induced positive charge on the electrode surface, thereby achieving electrostatic balance (step (iv)). Once the electrodes begin to approach the grid-like copper surface, electrostatic balance is

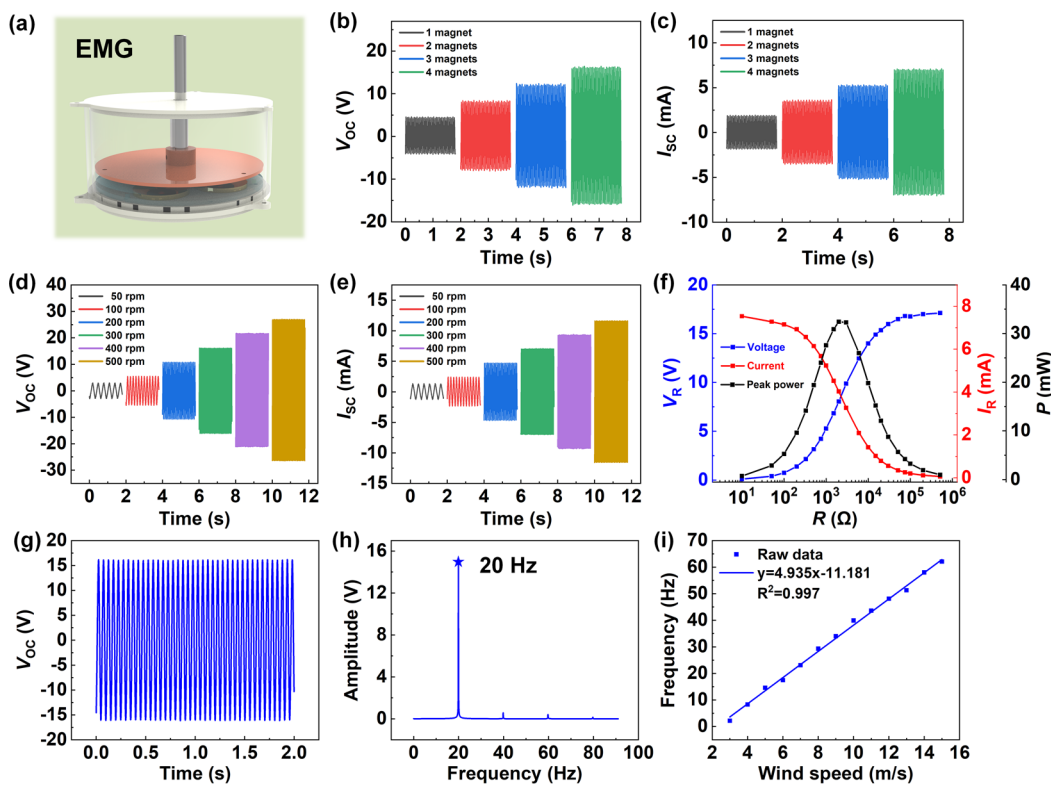


Figure 3. EMG part performance tests. (a) Schematic diagram of EMG. (b) V_{OC} and (c) I_{SC} of changing magnet number. (d) V_{OC} and (e) I_{SC} of EMG at different rotating speeds. (f) Voltage, current, and the peak power density of EMG change with different load resistance (300 rpm). (g) Original signal of EMG collected within 2 s and (h) result of FFT analysis on it. (i) Relationship among the signal frequency and wind speed.

achieved. Positive charges will flow out of the electrodes, creating a reverse current (step (v)). The periodic potential difference drives the electron flow along the ground and the electrode to neutralize the potential difference, thereby generating AC output voltage. To further study the theory of TENG, a finite element simulation of TENG is carried out using COMSOL (Figure 2d). The four-state potential distribution between copper and PTFE film is calculated.

Performances. Using a stepping motor as an excitation source to study the output characteristics of EMG, Figure 3a shows a schematic diagram of EMG part of ES-ETHG. Under the same rotating speed (300 rpm), the effect of the sum of magnets on open-circuit voltage (V_{OC}) and short-circuit current (I_{SC}) is confirmed in Figure 3b and c. As the number of magnets increases, the V_{OC} and I_{SC} of EMG increase. When numbers of magnets reach 4, the V_{OC} and I_{SC} will reach 16 V and 7.1 mA, respectively. In Figure S3, the output performance of coils in series and parallel is studied, with parallel connection proving easier to achieve high voltage at low speed. Figure 3d and e illustrate that the output performance of EMG increases with the increase in speed; as the speed increases from 50 to 500 rpm, V_{OC} increases from 3 to 27 V, and I_{SC} increases from 1.4 mA to 11.6 mA. The stability of EMG is tested, and there is no significant performance degradation of EMG after 6 h (Figure S4a). The performance of EMG can be studied in actual work, and the V_{OC} , I_{SC} , and peak power are tested under different load resistance. The V_{OC} increases and the I_{SC} decreases as the load resistance increases. When the load resistance is 2 k Ω , the maximum peak power is 32.4 mW (Figure 3f). The number of cycles of the electrical signal at the same time increases as the speed increases. Take the voltage

signal within 2 s at 300 rpm as an example (Figure 3g). Fast Fourier transform (FFT) calculation is performed on the voltage signal to accurately obtain the frequency of the voltage waveform (Figure 3h). FFT calculation is performed on voltage signals of different speeds, and the corresponding frequency information is obtained, respectively. As the speed increases, the frequency of the voltage signal also increases, so it can be used to describe the speed information. With the wind speed increasing from 3 to 15 m/s, the frequency of voltage increases from 2.2 to 62.1 Hz. The result demonstrates that the frequency of EMG increases almost linearly as the wind speed increases (Figure 3i). This excellent linear relationship illustrates that EMG can be invoked as a wind speed sensor to accurately measure the size of the wind speed.

To illustrate the capability of TENG-based wind direction sensor, the voltage output performance of the three electrodes at the same rotating speed is measured. Using a stepping motor to replace the wind vane, the speed was reduced by a speed of 1 rpm, and the voltage signals of three channels were obtained (Figure 4a). In Figure 4b, the peak V_{OC} of the three channels reached 5, 9, and 13 V, respectively. The three electrodes show a similar voltage waveform. When the electrodes move from the blank position to the copper foil position, V_{OC} increases in a positive direction. Then V_{OC} has a maximum value when the electrode and the copper foil are directly facing each other. When the electrode is entirely separated from the copper foil, V_{OC} has a minimum value. Therefore, when the electrode is in the position where the copper foil is installed on the grid, the voltage appears to change waveform periodically. When the electrode is completely separated from the grid-like copper foil, V_{OC} drops by a large margin. Because the angular velocity of

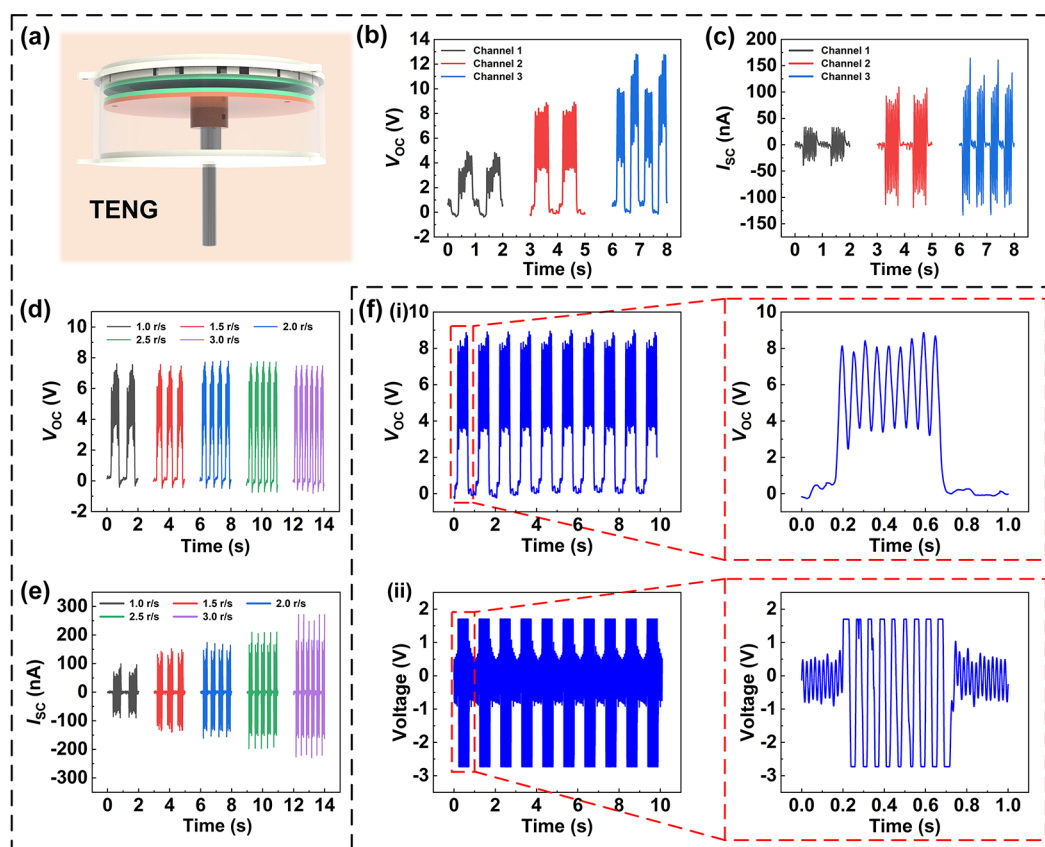


Figure 4. TENG part performance test. (a) Schematic diagram of TENG. (b) V_{OC} and (c) I_{SC} of different electrodes at rotating speeds of 1 r/s. (d) V_{OC} and (e) I_{SC} of electrode of different rotating speeds. (f) Waveform (i) before signal conditioning and (ii) after signal conditioning.

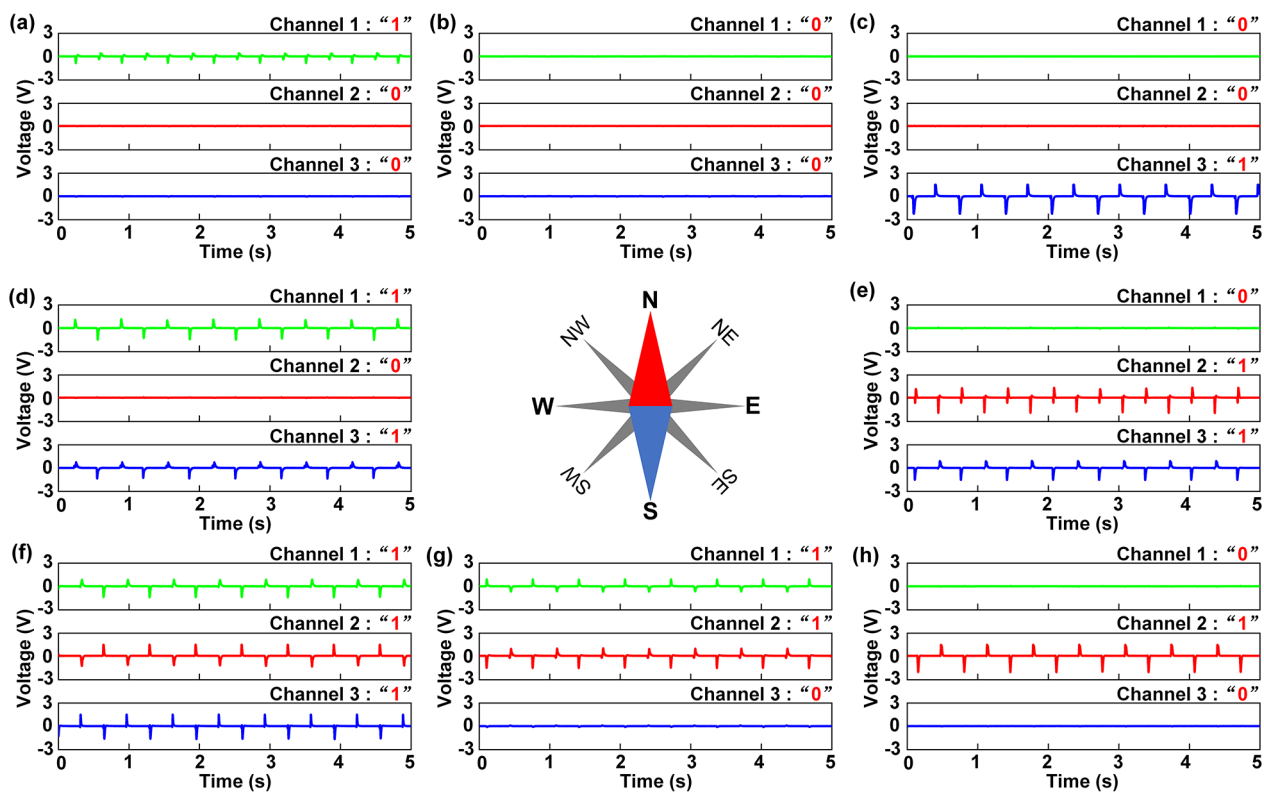


Figure 5. Measure the wind direction using TENG. Waveforms of the three channels when the wind direction is (a) northwest, (b) north, (c) northeast, (d) west, (e) east, (f) southwest, (g) south, and (h) southeast.

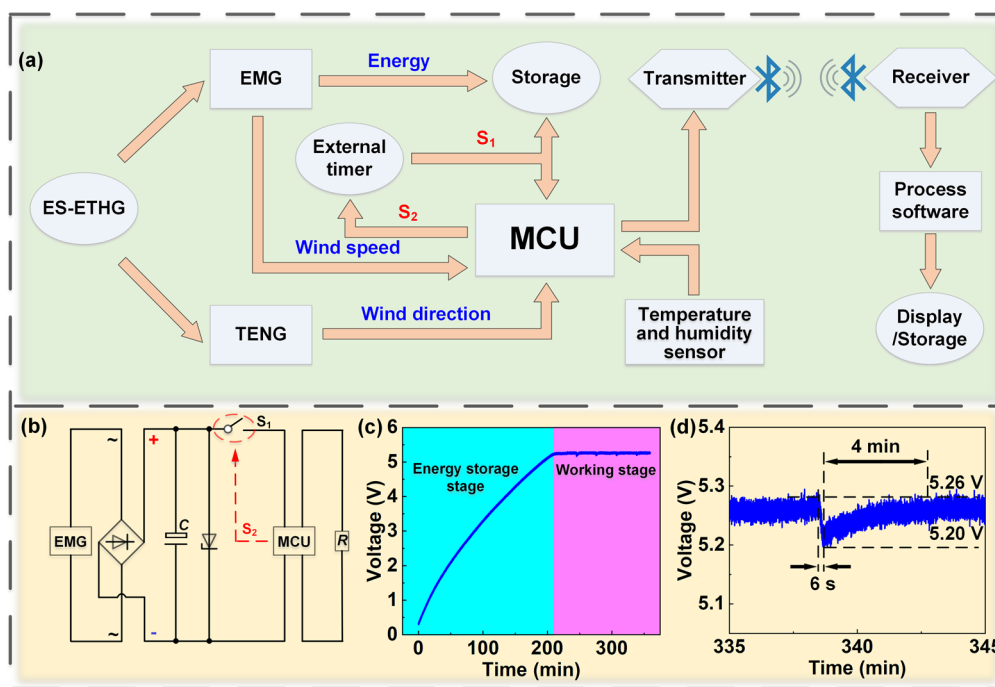


Figure 6. System construction of SDWS. (a) System structure of SDWS powered by ES-ETHG. (b) Structure of power management circuit. (c) Charging and discharging voltage curve of 10 F supercapacitor, which is used to provide power to the wirelessly transmit sensor data to the computer. (d) Voltage curve in a cycle.

the three channels is the same one and the radius increases in turn, the electrode area increases in turn leading to a rising trend of V_{OC} of the three channels. As shown in Figure 4c, the peak currents of the three channels are 34 nA, 100 nA, and 164 nA, respectively. I_{SC} of the three channels will only be generated when the electrodes pass through the grid-like copper foil. To test the performance of the electrode at different rotating speeds, V_{OC} remains at about 7.5 V unchanged (Figure 4d), and the peak current magnitude increases from 100 nA to 270 nA as the speed increases (Figure 4e). The value of I_{SC} depends on the amount of charge transferred per unit time, which is determined by the area of electrode. The magnitude of I_{SC} depends on the amount of the transferred charge per cycle. When the amount of transferred charge is unchanged, the faster the speed, the greater the current. The TENG demonstrates excellent output stability in a 3 h durability test (Figure S4b). When using an MCU, the internal resistance of the MCU is smaller than the internal resistance of the electrometer, and the TENG signal cannot be accurately measured, so three signal amplifiers (AD620) are used to translate the origin signal [Figure 4f(i)] into a square wave-like waveform [Figure 4f(ii)] for signal processing and analysis by MCU.

Wind direction is an important aspect of wind information. The application of TENG in self-powered wind sensor is demonstrated in Figure 5. Modern wind vanes are usually simple arrows. Here, a small flag is fixed at the tail of arrow. The wind vanes sway near the direction of the wind due to the oscillation under wind of the flexible flag. The three channels in the TENG generate electrical signals when the swing is transmitted to the TENG through the rotating shaft. Each time, the voltage waveforms of the three channels in the past 2 s are recorded by MCU. When electrodes move between the interdigital electrodes, the output signal will have a peak voltage greater than the threshold voltage of 1.5 V, which can

be recorded as “1”. When the peak voltage is less than the threshold voltage, it is recorded as “0”. The voltage information on the three channels can represent 8 wind directions after being encoded by Gray code (Figure 5a–h, Table S1). In Figure 5b, the peak voltage of each channel is less than the threshold voltage. It links to the code “000”. The corresponding AC voltages of the three channels can be recorded in one cycle at the same time when the wind vane rotates clockwise (Figure S5). The results show that TENG can effectively sense wind direction through signal processing and coding of voltage peaks.

An appropriate circuit is designed to SDWS for smart agriculture in Figure 6a. First, the electric energy of ES-ETHG is rectified and stabilized by the power management circuit and then stored in the capacitor or battery (Figure 6b). The original electrical signal is converted into direct current through full-bridge rectification, and then the high voltage signal is filtered through the Zener diode to stabilize the voltage of the farad capacitor at 5.26 V, avoiding the high voltage from causing damage to the electronic components (Figure S6). The power management circuit and signal processing unit are connected with EMG in parallel. The signal of TENG is directly received by the low-power MCU (STM32F103) after passing the amplifier and then, to ensure the normal operation of the system, an energy storage unit, an external timer (TPLS110), and an MCU. MCU is in charge of measuring, processing information, and wireless transmission in the system. The external timer is responsible for controlling the capacitor or battery to supply power to the MCU at fixed intervals. That said, the EMG can store irregular wind energy to provide adequate power when MCU is working. First, the supercapacitor was charged to 5.26 V by EMG at a rotating speed of 300 rpm (Figure 6c). Subsequently, the external timer is utilized to control the stored energy to supply power to the test system through the switch S_1 , and the information is

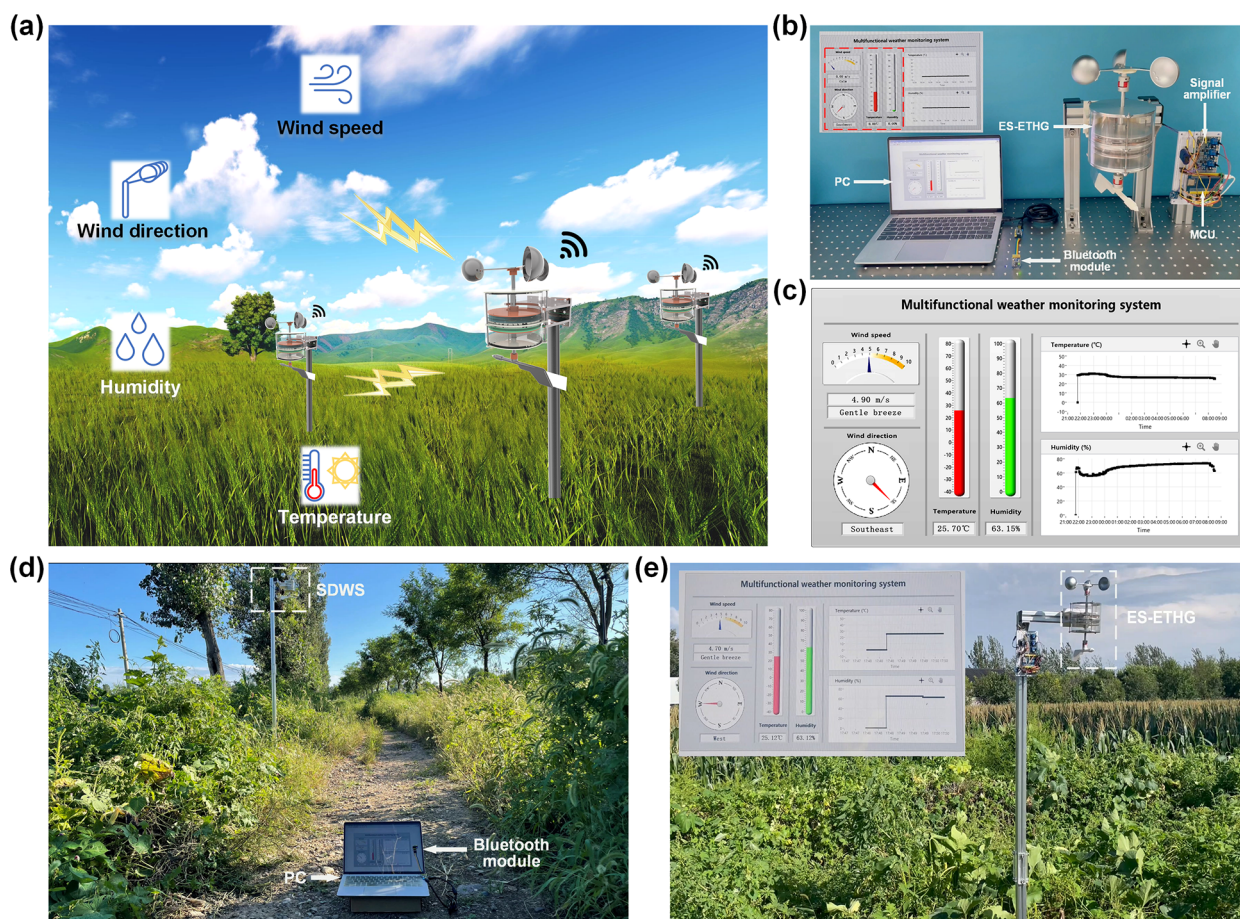


Figure 7. Demonstration of SDWS. (a) Conceptual diagram of SDWS. (b) Signal is transmitted through the Bluetooth module. (c) Remote weather monitoring demonstration program running panel. (d) SDWS is installed on the edge of farmland and (e) demonstrates weather monitoring.

transmitted wirelessly through Bluetooth communication after the measurement is completed. After the transmission is completed, the MCU will send a high level to the external timer to turn off the power supply through switch S_2 . In a working cycle including acquisition and transmission, the supercapacitor discharges to about 5.20 V in about 6 s (Figure 6d). During the operation of a functional unit, the stored energy of supercapacitor is reduced by approximately 1.14%. Compared with the initial charge cycle, the additional charge cycle takes about 4 min to fully charge the capacitor. While the EMG signal is charged to the capacitor through the power management circuit, the original signal is calculated by the MCU at the same time.

Demonstration. The SDWS can be used to collect real-time weather information in farmland such as wind speed, wind direction, temperature, humidity, and so on (Figure 7a). Figure 7b shows the overall system diagram integrated with the remote information transmission module. The system is primarily composed of a computer, MCU, and signal amplifier. To receive the SDWS signal, a Bluetooth transmitter is used, and a desktop smart agricultural meteorological collection program is developed based on LabVIEW (Figure 7c). The program can display the wind speed and direction in real time and calculate the wind speed rating based on the wind speed value. Real-time wind speed monitoring can remind producers to take preventive measures to prevent crop losses in a windy environment, which is of positive significance to agricultural

production. The system can also receive real-time temperature and humidity information from SDWS and plot the temperature and humidity information into a spreadsheet for historical tracking of temperature and humidity (Movie S1). To illustrate the operation of the equipment in the natural environment, SDWS is fixed on the edge of the farmland for signal transmission (Figure 7d,e, Movie S2). To investigate the effect of the harsh outdoor environment on the performance of the ES-ETHG, the ES-ETHG was placed in a constant temperature and humidity test chamber for performance testing at different humidity levels. The ES-ETHG does not suffer from any degradation in output performance due to changes in relative humidity between 30 and 90% (Figure S7). This may be due to the effective isolation of the TENG from the external environment by the shell. The intelligent agricultural sensing system based on ES-ETHG provides a driving force for agricultural production.

CONCLUSIONS

In summary, a method of integrating EMG and TENG in the IoT node to realize the self-powered IoT nodes and system is explored. ES-ETHG based on EMG and TENG has been constructed. EMG is used to collect energy and measure wind speed as a self-powered sensor. The wind speed has a linear relationship with the frequency of EMG signal and can accurately measure wind speed information. Using the TENG-based direction sensor as a self-powered wind direction sensor

can reduce the overall power consumption of system. Through demonstration experiments, the SDWS integrated with an energy management circuit, a low-power MCU, and a wireless transmission can measure the wind speed, wind direction, temperature, and humidity of farmland. It can be arranged in a complex agricultural production environment freely and flexibly, without additional cables or batteries. This work is a feasible approach to solve the power supply of IoT nodes and sensors. The self-powered IoT sensor network for smart agriculture provides a solution to make agriculture more efficient and captivating.

EXPERIMENTAL SECTION

Fabrication of ES-ETHG. ES-ETHG is composed of EMG and TENG. The shafts, rotors, and stators of EMG and TENG are lathe machined. Magnets and coils are mounted on the rotor and stator through acrylic plates. The thickness of the magnet is 3 mm, and the numbers of coil turns are 2000. The shell is cut out of an acrylic cylinder. The thickness of PTFE film on the stator electrode of TENG part is 0.13 mm, and the width of copper foil on the rotor is 10 mm. The copper foil is pasted on the circular acrylic plate, and the angle difference between the two copper foils on the grid-like copper is 10° . The acrylic plate is fixed on the rotor by screws.

Electrical Measurement. A stepper motor (J5718HBS401, China) is used to drive wind speed sensor and wind direction sensor when testing different rotating speeds. The electrical output performance of the ES-ETHG, such as open circuit voltage and short circuit current testing, is performed by a programmable electrometer (6514, Keithley, USA). The performance test of ES-ETHG with different relative humidity is performed in a constant temperature and humidity test chamber (Y-HF-960L, Yuhang Zhida, China). In the demonstration, wind speed data and temperature and humidity information are received and calculated directly by the MCU (STM32F103, China), and wind direction data are processed by three signal amplifiers (AD620, China) and then processed by the MCU. Temperature and humidity information is collected by a THS (SHT20, China). The signal is transmitted to the computer through the Bluetooth module (ATK-BLE01, China) and is processed and recorded by LabVIEW. The photos of the above components are depicted in Figure S8.

ASSOCIATED CONTENT

Supporting Information

The Supporting Information is available free of charge at <https://pubs.acs.org/doi/10.1021/acsnano.1c08417>.

The schematic flowchart for fabricating the ES-ETHG; effect of distance between magnet and coil on EMG performance; influence of connection mode on EMG at speed of 300 rpm; stability test of ES-ETHG; waveform transformation process of EMG; correspondence between wind direction and signal in a cycle; effect of relative humidity on the output performance of ES-ETHG; photo of electronic components in the circuit; coding process of wind direction (PDF)

Demonstration of remote self-powered weather sensing system (MP4)

Testing of remote self-powered weather sensing system outdoors (MP4)

AUTHOR INFORMATION

Corresponding Authors

Zhong Lin Wang – Beijing Institute of Nanoenergy and Nanosystems, Chinese Academy of Sciences, Beijing 101400, China; School of Nanoscience and Technology, University of Chinese Academy of Sciences, Beijing 100049, China;

CUSTech Institute of Technology, Wenzhou, Zhejiang 325024, China; School of Materials Science and Engineering, Georgia Institute of Technology, Atlanta, Georgia 30332-0245, United States; orcid.org/0000-0002-5530-0380; Email: zhong.wang@mse.gatech.edu

Tinghai Cheng – Beijing Institute of Nanoenergy and Nanosystems, Chinese Academy of Sciences, Beijing 101400, China; School of Nanoscience and Technology, University of Chinese Academy of Sciences, Beijing 100049, China; CUSTech Institute of Technology, Wenzhou, Zhejiang 325024, China; orcid.org/0000-0003-0335-7614; Email: chengtinghai@binn.cas.cn

Authors

Baosen Zhang – Beijing Institute of Nanoenergy and Nanosystems, Chinese Academy of Sciences, Beijing 101400, China; School of Nanoscience and Technology, University of Chinese Academy of Sciences, Beijing 100049, China; orcid.org/0000-0003-1747-8636

Sheng Zhang – Beijing Institute of Nanoenergy and Nanosystems, Chinese Academy of Sciences, Beijing 101400, China; School of Nanoscience and Technology, University of Chinese Academy of Sciences, Beijing 100049, China

Wenbo Li – Beijing Institute of Nanoenergy and Nanosystems, Chinese Academy of Sciences, Beijing 101400, China; School of Nanoscience and Technology, University of Chinese Academy of Sciences, Beijing 100049, China

Qi Gao – Beijing Institute of Nanoenergy and Nanosystems, Chinese Academy of Sciences, Beijing 101400, China; School of Nanoscience and Technology, University of Chinese Academy of Sciences, Beijing 100049, China

Da Zhao – Beijing Institute of Nanoenergy and Nanosystems, Chinese Academy of Sciences, Beijing 101400, China

Complete contact information is available at:

<https://pubs.acs.org/10.1021/acsnano.1c08417>

Author Contributions

[†]Baosen Zhang and Sheng Zhang contributed equally to this work.

Notes

The authors declare no competing financial interest.

ACKNOWLEDGMENTS

The authors are grateful for the supports received from the National Key R&D Project from the Minister of Science and Technology (2016YFA0202701 and 2016YFA0202704) and the Beijing Municipal Science and Technology Commission (Z171100002017017).

REFERENCES

- (1) Yin, H. Y.; Cao, Y. T.; Marelli, B.; Zeng, X. Q.; Mason, A. J.; Cao, C. Y. Soil Sensors and Plant Wearables for Smart and Precision Agriculture. *Adv. Mater.* **2021**, *33*, 2007764.
- (2) Basso, B.; Antle, J. Digital Agriculture to Design Sustainable Agricultural Systems. *Nat. Sustain.* **2020**, *3*, 254–256.
- (3) Giraldo, J. P.; Wu, H. H.; Newkirk, G. M.; Kruss, S. Nanobiotechnology Approaches for Engineering Smart Plant Sensors. *Nat. Nanotechnol.* **2019**, *14*, 541–553.
- (4) Reba, M.; Seto, K. C. A Systematic Review and Assessment of Algorithms to Detect, Characterize, and Monitor Urban Land Change. *Remote Sens. Environ.* **2020**, *242*, 111739.
- (5) Devaraju, J. T.; Suhas, K. R.; Mohana, H. K.; Patil, V. A. Wireless Portable Microcontroller Based Weather Monitoring Station. *Measurement* **2015**, *76*, 189–200.

- (6) Ruan, J.; Jiang, H.; Zhu, C.; Hu, X.; Shi, Y.; Liu, T.; Rao, W.; Chan, F. T. S. Agriculture IoT: Emerging Trends, Cooperation Networks, and Outlook. *IEEE Wirel. Commun.* **2019**, *26*, 56–63.
- (7) Hittinger, E.; Jaramillo, P. Internet of Things: Energy Boon or Bane? *Science* **2019**, *364*, 326.
- (8) Chen, B.; Yang, Y.; Wang, Z. L. Scavenging Wind Energy by Triboelectric Nanogenerators. *Adv. Energy Mater.* **2018**, *8*, 1702649.
- (9) Liu, S. M.; Li, X.; Wang, Y. Q.; Yang, Y. F.; Meng, L. X.; Cheng, T. H.; Wang, Z. L. Magnetic Switch Structured Triboelectric Nanogenerator for Continuous and Regular Harvesting of Wind Energy. *Nano Energy* **2021**, *83*, 105851.
- (10) Wang, M.; Zhang, J. H.; Tang, Y. J.; Li, J.; Zhang, B. S.; Liang, E. J.; Mao, Y. C.; Wang, X. D. Air-Flow-Driven Triboelectric Nanogenerators for Self-Powered Real-Time Respiratory Monitoring. *ACS Nano* **2018**, *12*, 6156–6162.
- (11) Zhang, L.; Zhang, B. B.; Chen, J.; Jin, L.; Deng, W. L.; Tang, J. F.; Zhang, H. T.; Pan, H.; Zhu, M. H.; Yang, W. Q.; Wang, Z. L. Lawn Structured Triboelectric Nanogenerators for Scavenging Sweeping Wind Energy on Rooftops. *Adv. Mater.* **2016**, *28*, 1650–1656.
- (12) Liang, X.; Jiang, T.; Liu, G. X.; Feng, Y. W.; Zhang, C.; Wang, Z. L. Spherical Triboelectric Nanogenerator Integrated with Power Management Module for Harvesting Multidirectional Water Wave Energy. *Energy Environ. Sci.* **2020**, *13*, 277–285.
- (13) Zhao, X. J.; Kuang, S. Y.; Wang, Z. L.; Zhu, G. Highly Adaptive Solid-Liquid Interfacing Triboelectric Nanogenerator for Harvesting Diverse Water Wave Energy. *ACS Nano* **2018**, *12*, 4280–4285.
- (14) Wang, Z. L. Triboelectric Nanogenerators as New Energy Technology and Self-Powered Sensors - Principles, Problems and Perspectives. *Faraday Discuss.* **2014**, *176*, 447–458.
- (15) Tarancón, A. Powering the IoT Revolution with Heat. *Nat. Electron.* **2019**, *2*, 270–271.
- (16) Chen, J.; Zhu, G.; Yang, W. Q.; Jing, Q. S.; Bai, P.; Yang, Y.; Hou, T. C.; Wang, Z. L. Harmonic-Resonator-Based Triboelectric Nanogenerator as a Sustainable Power Source and a Self-Powered Active Vibration Sensor. *Adv. Mater.* **2013**, *25*, 6094–6099.
- (17) Zhu, Y. Z.; Tian, M.; Chen, Y.; Yang, Y. J.; Liu, X. P.; Gao, S. Y. 3D Printed Triboelectric Nanogenerator Self-Powered Electro-Fenton Degradation of Orange IV and Crystal Violet System Using N-Doped Biomass Carbon Catalyst with Tunable Catalytic Activity. *Nano Energy* **2021**, *83*, 105824.
- (18) Zhong, Y. M.; Zhao, H. B.; Guo, Y. C.; Rui, P. S.; Shi, S. W.; Zhang, W.; Liao, Y. L.; Wang, P. H.; Wang, Z. L. An Easily Assembled Electromagnetic-Triboelectric Hybrid Nanogenerator Driven by Magnetic Coupling for Fluid Energy Harvesting and Self-Powered Flow Monitoring in a Smart Home/City. *Adv. Mater. Technol.* **2019**, *4*, 1900741.
- (19) Fan, F.-R.; Tian, Z.-Q.; Wang, Z. L. Flexible Triboelectric Generator. *Nano Energy* **2012**, *1*, 328–334.
- (20) Wang, Z. L. Triboelectric Nanogenerators as New Energy Technology for Self-Powered Systems and as Active Mechanical and Chemical Sensors. *ACS Nano* **2013**, *7*, 9533–9557.
- (21) Islam, E.; Abdullah, A. M.; Chowdhury, A. R.; Tasnim, F.; Martinez, M.; Olivares, C.; Lozano, K.; Uddin, M. J. Electromagnetic-Triboelectric-Hybrid Energy Tile for Biomechanical Green Energy Harvesting. *Nano Energy* **2020**, *77*, 105250.
- (22) Wang, P. H.; Pan, L.; Wang, J. Y.; Xu, M. Y.; Dai, G. Z.; Zou, H. Y.; Dong, K.; Wang, Z. L. An Ultra-Low-Friction Triboelectric-Electromagnetic Hybrid Nanogenerator for Rotation Energy Harvesting and Self-Powered Wind Speed Sensor. *ACS Nano* **2018**, *12*, 9433–9440.
- (23) Wu, C. S.; Wang, A. C.; Ding, W. B.; Guo, H. Y.; Wang, Z. L. Triboelectric Nanogenerator: A Foundation of the Energy for the New Era. *Adv. Energy Mater.* **2019**, *9*, 1802906.
- (24) Wang, Z. L.; Jiang, T.; Xu, L. Toward the Blue Energy Dream by Triboelectric Nanogenerator Networks. *Nano Energy* **2017**, *39*, 9–23.
- (25) Zi, Y. L.; Wang, J.; Wang, S. H.; Li, S. M.; Wen, Z.; Guo, H. Y.; Wang, Z. L. Effective Energy Storage from a Triboelectric Nanogenerator. *Nat. Commun.* **2016**, *7*, 10987.
- (26) Zhang, C.; Tang, W.; Han, C. B.; Fan, F. R.; Wang, Z. L. Theoretical Comparison, Equivalent Transformation, and Junction Operations of Electromagnetic Induction Generator and Triboelectric Nanogenerator for Harvesting Mechanical Energy. *Adv. Mater.* **2014**, *26*, 3580–3591.
- (27) Wang, Z. L. Nanogenerators, Self-Powered Systems, Blue Energy, Piezotronics and Piezo-Phototronics - A Recall on the Original Thoughts for Coining These Fields. *Nano Energy* **2018**, *54*, 477–483.
- (28) Wu, Y.; Jing, Q. S.; Chen, J.; Bai, P.; Bai, J. J.; Zhu, G.; Su, Y. J.; Wang, Z. L. A Self-Powered Angle Measurement Sensor Based on Triboelectric Nanogenerator. *Adv. Funct. Mater.* **2015**, *25*, 2166–2174.
- (29) Xiong, J. Q.; Cui, P.; Chen, X. L.; Wang, J. X.; Parida, K.; Lin, M. F.; Lee, P. S. Skin-Touch-Actuated Textile-Based Triboelectric Nanogenerator with Black Phosphorus for Durable Biomechanical Energy Harvesting. *Nat. Commun.* **2018**, *9*, 4280.
- (30) Jing, Q.; Zhu, G.; Bai, P.; Xie, Y. N.; Chen, J.; Han, R. P. S.; Wang, Z. L. Case-Encapsulated Triboelectric Nanogenerator for Harvesting Energy from Reciprocating Sliding Motion. *ACS Nano* **2014**, *8*, 3836–3842.
- (31) Zhang, B. S.; Tang, Y. J.; Dai, R. R.; Wang, H. Y.; Sun, X. P.; Qin, C.; Pan, Z. F.; Liang, E. J.; Mao, Y. C. Breath-Based Human-Machine Interaction System Using Triboelectric Nanogenerator. *Nano Energy* **2019**, *64*, 103953.
- (32) Rana, S. M. S.; Rahman, M. T.; Salauddin, M.; Maharjan, P.; Bhatta, T.; Cho, H.; Park, J. Y. A Human-Machine Interactive Hybridized Biomechanical Nanogenerator as a Self-Sustainable Power Source for Multifunctional Smart Electronics Applications. *Nano Energy* **2020**, *76*, 105025.
- (33) Wang, X.; Yang, Y. Effective Energy Storage from a Hybridized Electromagnetic-Triboelectric Nanogenerator. *Nano Energy* **2017**, *32*, 36–41.
- (34) Zhong, X. D.; Yang, Y.; Wang, X.; Wang, Z. L. Rotating-Disk-Based Hybridized Electromagnetic-Triboelectric Nanogenerator for Scavenging Biomechanical Energy as a Mobile Power Source. *Nano Energy* **2015**, *13*, 771–780.
- (35) Wang, X.; Wang, S. H.; Yang, Y.; Wang, Z. L. Hybridized Electromagnetic-Triboelectric Nanogenerator for Scavenging Air-Flow Energy to Sustainably Power Temperature Sensors. *ACS Nano* **2015**, *9*, 4553–4562.
- (36) Cao, R.; Zhou, T.; Wang, B.; Yin, Y. Y.; Yuan, Z. Q.; Li, C. J.; Wang, Z. L. Rotating-Sleeve Triboelectric-Electromagnetic Hybrid Nanogenerator for High Efficiency of Harvesting Mechanical Energy. *ACS Nano* **2017**, *11*, 8370–8378.
- (37) Wang, P. H.; Liu, R. Y.; Ding, W. B.; Zhang, P.; Pan, L.; Dai, G. Z.; Zou, H. Y.; Dong, K.; Xu, C.; Wang, Z. L. Complementary Electromagnetic-Triboelectric Active Sensor for Detecting Multiple Mechanical Triggering. *Adv. Funct. Mater.* **2018**, *28*, 1705808.